



CHORUS

This is the accepted manuscript made available via CHORUS. The article has been published as:

Correlation Between Corrugation-Induced Flexoelectric Polarization and Conductivity of Low-Dimensional Transition Metal Dichalcogenides

Anna N. Morozovska, Eugene A. Eliseev, Hanna V. Shevliakova, Yaroslava Yu. Lopatina, Galina I. Dovbeshko, Maya D. Glinchuk, Yunseok Kim, and Sergei V. Kalinin

Phys. Rev. Applied **15**, 044051 — Published 29 April 2021

DOI: [10.1103/PhysRevApplied.15.044051](https://doi.org/10.1103/PhysRevApplied.15.044051)

Notice: This manuscript has been authored by UT-Battelle, LLC, under Contract No. DE-AC0500OR22725 with the U.S. Department of Energy. The United States Government retains and the publisher, by accepting the article for publication, acknowledges that the United States Government retains a non-exclusive, paid up, irrevocable, world-wide license to publish or reproduce the published form of this manuscript, or allow others to do so, for the United States Government purposes. The Department of Energy will provide public access to these results of federally sponsored research in accordance with the DOE Public Access Plan (<http://energy.gov/downloads/doe-public-access-plan>).

Correlation between corrugation-induced flexoelectric polarization and conductivity of low-dimensional transition metal dichalcogenides

Anna N. Morozovska^{1*}, Eugene A. Eliseev², Hanna V. Shevliakova^{1,3}, Yaroslava Yu. Lopatina¹, Galina I. Dovbeshko¹, Maya D. Glinchuk², Yunseok Kim^{4†}, and Sergei V. Kalinin^{5,‡}

*¹Institute of Physics, National Academy of Sciences of Ukraine,
46, pr. Nauky, 03028 Kyiv, Ukraine*

*²Institute for Problems of Materials Science, National Academy of Sciences of Ukraine,
Krjijanovskogo 3, 03142 Kyiv, Ukraine*

*³Department of Microelectronics, National Technical University of Ukraine “Igor Sikorsky Kyiv
Polytechnic Institute”, Kyiv, Ukraine*

*⁴School of Advanced Materials Science and Engineering, Sungkyunkwan University (SKKU), Suwon
16419, Republic of Korea*

*⁵The Center for Nanophase Materials Sciences, Oak Ridge National Laboratory, Oak Ridge, TN
37922*

* Corresponding author 1: anna.n.morozovska@gmail.com

† Corresponding author 2: yunseokkim@skku.edu

‡ Corresponding author 3: sergei2@ornl.gov

Abstract

Tunability of polar and semiconducting properties of low-dimensional transition metal dichalcogenides (TMDs) have propelled them to the forefront of fundamental and applied physical research. These materials can vary their electrophysical properties from non-polar to ferroelectric, and from direct-band semiconducting to metallic. In addition to classical controlling factors such as field effect, composition, and doping, new degrees of freedom emerge in TMDs due to the curvature-induced electron redistribution and associated changes of electronic properties.

Here we theoretically explore the elastic and electric fields, flexoelectric polarization and free charge density for a TMD nanoflake placed on a rough substrate with a sinusoidal profile of the corrugation. Finite element modelling results for different flake thickness and corrugation depth yield insight into the flexoelectric nature of the out-of-plane electric polarization and establish the unambiguous correlation between the polarization and static conductivity modulation. The modulation is caused by the coupling between deformation potential and inhomogeneous elastic strains, which evolve in TMD nanoflake due to the adhesion between the flake surface and corrugated substrate.

We revealed a pronounced maximum at the thickness dependences of the electron and hole conductivity of MoS₂ and MoTe₂ nanoflakes placed on a corrugated substrate, which opens the way for their geometry optimization towards significant improvement their polar and electronic properties, necessary for advanced applications in nanoelectronics and memory devices. Specifically, obtained results can be useful for elaboration of nanoscale straintronic devices based on the bended MoS₂, MoTe₂ and MoSTe nanoflakes, such as diodes and bipolar transistors with a bending-controllable sharpness of p-n junctions.

I. INTRODUCTION

Tunability of polar and semiconducting properties of low-dimensional (**LD**) transition metal dichalcogenides (**TMDs**) with a chemical formula MX_2 (M – metal Mo, W, Re; X – chalcogen S, Se, Te) [1, 2] and Janus-compounds (**JC**) with a chemical formula MXY (X, Y – chalcogens) [3, 4, 5] in the form of monolayers and nanoflakes have propelled them to the forefront of fundamental and applied physical research. These materials offer a broad gamut of properties varying from non-polar to ferroelectric, and from direct-band semiconductor to metallic. Remarkably that LD semiconductor materials, such as graphene, MX_2 and MXY , are ideal candidates for the strain engineering [6] and straintronics [7], because its strain-induced conductive domain walls can act as mobile charged channels, similarly to the “domain wall nanoelectronics” in multiferroic thin films [8, 9, 10] and graphene-on-ferroelectric nanostructures [11, 12].

Layered TMDs in the form of bulk materials are typically non-polar centrosymmetric semiconductors with a relatively wide band gap $\sim(1.1 - 2)$ eV [1]. However, on transition from the bulk to the nanoscale additional orderings emerge. These orderings can be non-polar or piezoelectric, or even ferroelectric [13, 14, 15], semiconductive, semi-metallic or metallic [16, 17, 18], as are found in different structural phases (polymorphs) of TMD monolayers. Similarly, in addition to classical controlling factors, such as field effect, composition, and doping [19], new degrees of freedom emerge in TMDs due to the curvature-induced electron redistribution and associated changes in electronic properties (see e.g. [20, 21]). In particular, here are very prospective theoretical and experimental possibilities for tuning the structural, polar and electronic properties of LD-TMDs by application of homogeneous [22, 23] and inhomogeneous [24, 25] elastic strains. However, these possibilities are almost not systematized and mostly empirical.

From theoretical perspective, a number of first-principles studies explored the surface-induced piezoelectricity [26, 27] and ferroelectric polarization [15, 28] in various MX_2 . As predicted by several authors [21, 29], and later discovered experimentally [24], an elastic bending can induce polar phenomena in LD-TMDs, either intrinsic or induced by the external structural and charge disorder. Large curvatures enabled by small bending stiffnesses can give rise to a significant polarization induced by a flexoelectric effect [30, 31]. The bending-induced out-of-plane dipole moment with density $p \sim (0.01 - 0.4)\text{C/nm}$ and flexoelectric polarization $P \sim (0.1 - 2)\mu\text{C/cm}^2$ [32] were calculated from the first principles for MoS_2 [15], WS_2 [31], and WTe_2 [33, 34] single-layers, respectively. Therefore, it is quite possible that the strongly inhomogeneous spontaneous deformation of LD-TMD,

which causes the appearance of their spontaneous polarization, is due to the flexoelectric coupling [1, 24, 36]. Let us focus on several recent examples.

Previously, we describe analytically the structural phases of MX_2 and discuss the mechanisms of its ferroelectric state appearance using Landau-Ginzburg-Devonshire-type (**LGD-type**) approach [35]. The LGD-type thermodynamic analysis suggests that out-of-plane ferroelectricity can exist in many phases of LD-TMDs with a switchable polarization being proportional to the out-of-plane order parameter, and further predict that the domain walls in LD-TMDs should become conductive above a certain strain threshold. Despite the progress, the nature of one-dimensional piezoelectricity and ferroelectricity has not been elucidated, and the mesoscopic analytical theory of polar and electronic phenomena in LD-TMD has not been constructed. Such a theory is necessary to control and predict the physical properties of LD-TMD and JC for their novel applications in nanoelectronics and advanced memories.

From a crystallographic and symmetry point of view, only the in-plane piezoelectricity can exist in a geometrically flat centrosymmetric MX_2 layer. Even though symmetry, the tunable out-of-plane piezoelectricity induced by the local flexoelectricity was observed by Kang et al. [24] in semiconducting 2H-MoTe₂ flakes by creating the surface corrugation. The flexoelectricity induced by the surface corrugation can appear in other two-dimensional or thin-layered materials and, furthermore, the results could provide useful information on the interweaving nature between mechanical stimulus and electric dipole in low-dimensional materials. Next, Kang et al. [1] demonstrated the creation of strong out-of-plane piezoelectricity in semiconducting 2H-MoTe₂ flakes by an artificial atomic-scale symmetry breaking realized through Te vacancy formation, and confirmed by DFT calculations.

Recently [36] we developed LGD-type theory for the description of polar phenomena in LD-TMDs, specifically exploring flexoelectric origin of the polarization induced by a spontaneous bending and by inversion symmetry breaking due to the interactions with substrate. We consider the appearance of the spontaneous out-of-plane polarization due to the flexoelectric coupling with the strain gradient of the spontaneous surface rippling and surface-induced piezoelectricity in TMDs single-layers. Performed calculations proved that the out-of-plane spontaneous polarization, originated from the flexoelectric effect in a rippled TMD, is bistable and reversible by a non-uniform electric field.

This work is devoted to the establishment of correlation between polar and electronic properties of LD-TMDs and JCs, which is almost unexplored. Using finite element modeling (**FEM**) we calculate

the elastic and electric fields, flexoelectric polarization and free charge density for a TMD (or JC) nanoflake placed on a rough substrate with a sinusoidal profile of the corrugation. Analysis of FEM results obtained for the different flake thickness (varying from 10 to 300 nm in accordance with experiment [24]) and corrugation depth (varying from 0 to 50 nm according to typical technological conditions [37]), allows to corroborate the flexoelectric nature of the out-of-plane electric polarization and establish the unambiguous correlation between the polarization and static conductivity modulation.

II. THEORETICAL MODEL AND MATERIAL PARAMETERS

Here we explore the effect of bending-induced flexoelectric polarization of MX_2 nanoflakes originated from the adhesion to a corrugated substrate. For JCs, the flexoelectric polarization can be superposed with the piezoelectric polarization coming from inversion symmetry breaking at the MXY surface. The overall picture of the bending-induced flexoelectric polarization and surface-induced piezoelectric polarization in and MX_2 and MXY is shown schematically in **Fig. 1**.

A flat single-layer (**SL**) with a chemical formula MX_2 , where M is a transition metal, X is a chalcogenide is shown in **Fig. 1a**. Projections of M ions are located at the middle line between projections of X ions. The inhomogeneous strain is absent in a flat SL MX_2 . Since the effective (Born or Bader) charges Q of M and X ions are opposite, namely $Q_M = -2Q_X$, the total polarization is absent. For the case of a stretched flat Janus-compound with a chemical formula XMY , the top X and bottom Y chalcogen ions are in non-equivalent conditions despite their planes are parallel (see **Fig. 1d**). While the total charge is zero, $Q_M = -Q_X - Q_Y$, the surface-induced piezoelectric effect can induce surface dipoles. The dipoles are responsible for the nonzero total out-of-plane polarization P shown by a dashed black curve and arrows in **Fig. 1d**.

A mechanically free SL MX_2 and MXY , where all X, Y and M ions positions can spontaneously reconstruct to the rippled state with the lowest energy, are shown in **Fig. 1b** and **1f**, respectively. Since the force matrix [38] is different for the “light” X (or Y) and “heavy” M ions, the amplitudes of X (or Y) and M ions displacements are different for the periodic ripples. Since the total effective charge is absent, the periodic displacement of X (or Y) and M ions induces the out-of-plane polarization modulation (dashed black curve and arrows) due to the flexoelectric coupling only.

The flexoelectric coupling exists for all possible symmetries [44] and geometries of the TMD and JC; hence the effect always contributes to the total polarization, as shown in **Fig. 1b-1d** and **1f-1h**. The surface-induced piezoelectric effect contributes to the out-of-plane polarization of a SL MX_2 only for the case on non-equivalent conditions for the top and bottom chalcogen layers, that is the case of

one surface free and other clamped to a flat rigid substrate (see Fig. 1c). Since the top “Y” and bottom “X” chalcogen layers have different force matrices, the surface-induced piezoelectric effect always induces the out-of-plane polarization of a SL MXY (see Fig. 1e-1g).

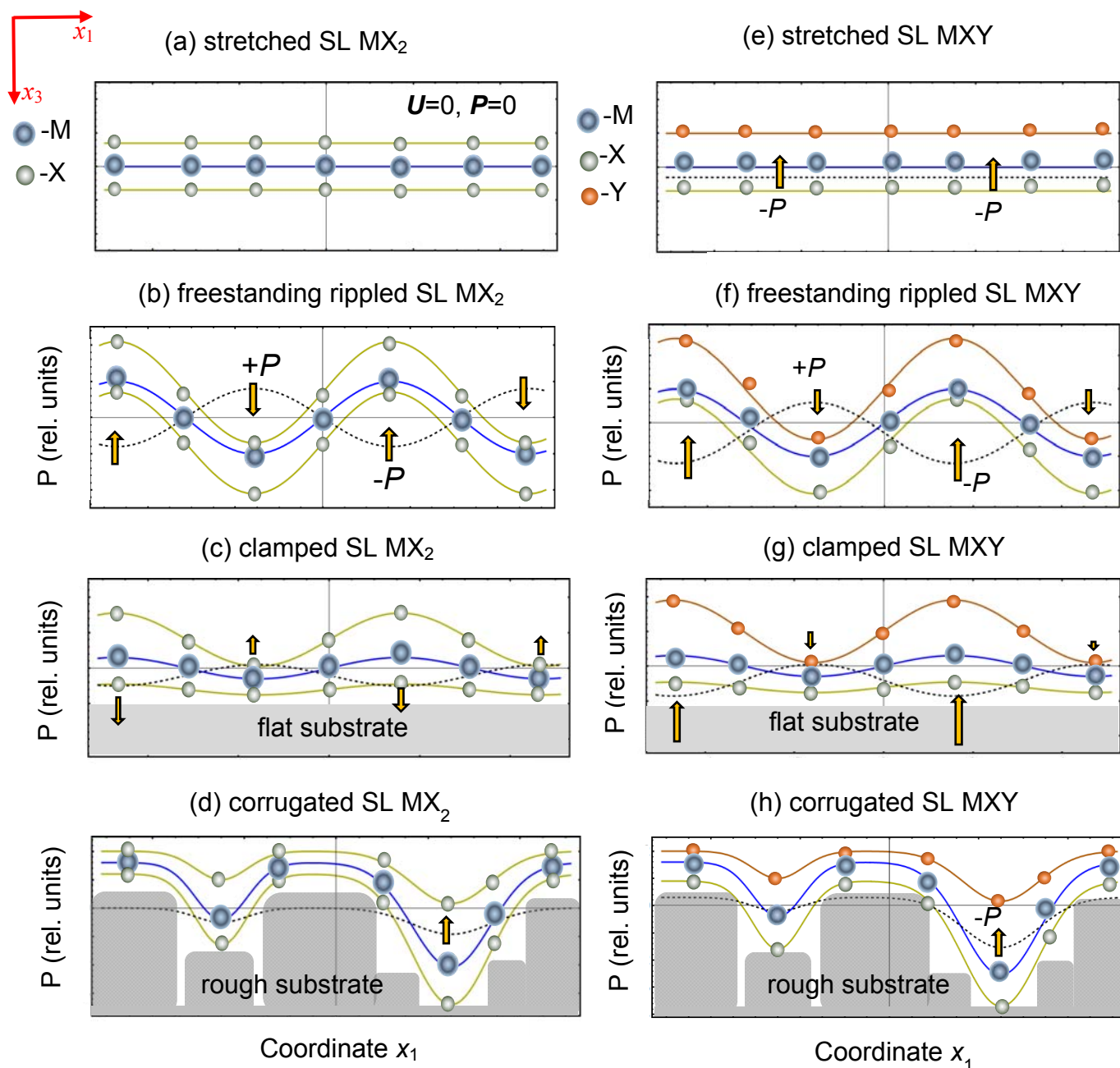


FIGURE 1. Bending-induced out-of-plane polarization in a SL MX₂ (a-d) and Janus compound YMX (e-h). M is a transition metal, X and Y are chalcogen atoms. M ions are positively charged, X and Y ions are negatively charged. Orange arrows indicate the direction of emerging out-of-plane dipole polarization P , which profile is shown by a dashed black curve. A relative atomic displacement U and out-of-plane polarization P are

absent for a flat stretched SL MX₂ (**a**); and a small uniform P can appear for YMX (**e**). A freestanding SL MX₂ (**b**) and MXY (**f**). (**c**) Rippled and strained SL MX₂ (**c**, **d**) and MXY (**g**, **h**) clamped to a flat (**c,g**) or rough (**d,h**) rigid substrate. Parts (**a**)-(**c**) are reprinted from Ref. [36].

Since the bottom X ions are bonded to the substrate [39] by different types of van der Waals (**vdW**) forces [40, 41], in the case of strong adhesion [42, 43] they remained almost “clamped” to the atomic planes of a flat (e.g., atomically smooth) substrate or to the islands of atoms of a rough (e.g., corrugated) substrate. For the case of rough substrates used in e.g., experiments [1, 24] the inhomogeneous strain can exist in the clamped sections, while the suspended sections can relax freely (see **Fig. 1d** and **1h**). The amplitude of the clamped atoms vertical displacement is very small there, a more visible change of position is possible for the middle and top ions. A significant reconstruction occurs for the ions at “suspended” sections, where the different amplitudes of the displacement of bottom X, middle M ions and top X (or Y) ions induce the polarization (dashed black curve and arrows) due to the flexoelectric coupling in MX₂, and both flexoelectric coupling and surface-induced piezoelectric effect in MXY.

The out-of-plane polarization component P_3 [32] of a SL TMD (or JC) shown in **Figs. 1b-h** can be estimated by a continuum media approach [36], which is applicable even for ultrathin layers [23, 25], and becomes quantitative for the thicknesses more than 10 lattice constants [7-9]. Within the framework of a continuum media approach [36], P_3 comprises the flexoelectric and piezoelectric contributions. The first one is proportional to the second derivatives of elastic displacement in space and time multiplied by static and dynamic flexoelectric coefficients, respectively. The second one is proportional to surface-induced piezoelectric coefficient multiplied by an elastic strain. So:

$$P_3(\vec{x}, t) \cong f_{3jkl} \frac{\partial^2 U_j(\vec{x}, t)}{\partial x_k \partial x_l} - \mu_{3j} \frac{\partial^2 U_j(\vec{x}, t)}{\partial t^2} + \frac{e_{3jk}^s}{t} \frac{\partial U_j(\vec{x}, t)}{\partial x_k}. \quad (1)$$

Here $U_j(\vec{x})$ is the mechanical displacement of the flake, which includes a spontaneous and misfit contributions, f_{ijkl} is the static flexoelectric tensor [44] determined by the microscopic properties of the material [45, 46], μ_{ij} is the dynamic flexoelectric tensor [47], e_{ijk}^s is the tensor of the surface-induced piezoelectric effect [48, 49] measured in pC/m, and t is the flake thickness [50]. Einstein summation notation is used hereinafter.

It follows from the symmetry considerations, e_{3jk}^s is zero for a flat centrosymmetric MX₂ with inversion axis “3”, it was estimated as several -2.4 pC/m for a reconstructed SL-MoS₂ in 1T’ phase [15]. It is much higher ($e_{31}^s \sim 50$ pC/m) for an asymmetric Janus compound MoSTe [28, 33]. Both

these values are much smaller than in-plane components, $e_{1jk}^s \sim (300 - 500)$ pC/m, estimated for MoS₂, MoTe₂, and MoSTe [15, 28].

The linear partial differential equation relating the mechanical displacement $U_j(\vec{x})$ of the flake points and its elastic stress σ_{ij} has the form:

$$\rho \frac{\partial^2 U_i}{\partial t^2} + \frac{\partial}{\partial x_j} \sigma_{ij}(\vec{x}, t) = \mu_{ij} \frac{\partial^2 P_j}{\partial t^2} + \frac{\partial}{\partial x_i} \psi(\vec{x}, t), \quad (2)$$

where ρ is the density of material and $\psi(\vec{x}, t)$ is an elastic force density (with dimensionality N/m³) in the nanoflake. The physical origin of these forces can include the atomic reconstruction of the free surface, as well as adhesion (e.g., vdW force) to the flat or corrugated substrate. Within a continuum media approach, we used here, the force is given by a standard Lenard-Jones potential [40 – 43].

For a static case considered here, Eq.(1) reduces to

$$P_3(\vec{x}) \cong f_{3jkl} \frac{\partial}{\partial x_j} u_{kl}(\vec{x}) + \frac{e_{3jk}^s}{t} u_{jk}(\vec{x}), \quad (3a)$$

where $u_{kl} = \frac{1}{2} \left(\frac{\partial U_k}{\partial x_l} + \frac{\partial U_l}{\partial x_k} \right)$ is an elastic strain tensor. The coupling between the stress σ_{ij} and strain u_{kl} is given by the generalized Hooke's law [51],

$$\sigma_{ij} = c_{ijkl} u_{kl} + F_{ijmn} \frac{\partial P_m}{\partial x_n} + h_{3ij}^s P_3 \approx c_{ijkl} u_{kl} + O \left(f_{3ij}^2, (h_{3ij}^s)^2 \right), \quad (3b)$$

where c_{ijkl} is the tensor of elastic stiffness, F_{ijmn} is a flexoelectric tensor (in V), and h_{mij}^s is a surface-induced piezoelectric stress tensor (in V), which is absent for a centrosymmetric MX₂ and present for Janus MXY. The approximate equality is the decoupling approximation, valid for small flexoelectric and surface piezoelectric effects, which are indeed small in the considered case.

Using the decoupling approximation in Eq.(3b), Eq.(2) yields Lamé equation:

$$c_{ijkl} \frac{\partial^2 U_k(\vec{x})}{\partial x_j \partial x_l} = \frac{\partial}{\partial x_i} \psi(\vec{x} - \vec{x}_s), \quad (3c)$$

where \vec{x}_s is the corrugation profile of a rough substrate (see **Fig. 2**).

To solve Eq. (3c), we need to define the adhesion force $\psi(\vec{x})$ between the layers of X, M or/and Y atoms, and an atomically flat or corrugated substrate. Here we use the assumption that the constitutive parts of vdW forces [40] corresponding to dipole-dipole, and dispersive-dipole interactions and London dispersive force, determine the atomic repulsion at ultra-small distances, and their attraction at higher distances. In this approximation, the adhesion force (per unit volume, in J/m³) between the flake and substrate can be approximated by a power law attraction with a prefactor – contact adhesive stiffness S_A at distances $|\vec{x} - \vec{x}_s| > \delta h_0$, and strong repulsion at distances $|\vec{x} - \vec{x}_s| <$

δh_0 (see also **Appendix A** in **Suppl. Mat.** [52]). The force characteristics, namely adhesive stiffness and repulsive separation, should be implemented in the software used for FEM.

Using FEM, performed in COMSOL@MultiPhysics software (see details in **Appendix B** [52]), we analyze the scenario, when TMD nanoflakes are placed on a rough substrate with an ideal 1D sinusoidal corrugation profile $\vec{x}_s = \left\{0, 0, A \cos\left(\frac{2\pi}{\lambda} x_1\right)\right\}$ corresponding to the case of perfect 1D ripples. Thus, we consider an ideal 2D problem, when all physical variables are regarded dependent on the in-plane coordinate x_1 and out-of-plane coordinate x_3 , but are independent on other in-plane the coordinate x_2 .

For sufficiently strong adhesion forces, the flake displacement, strain, strain gradient, and out-of-plane electric polarization (1) are modulated by the corrugation profile, being maximal at the corrugation peaks and minimal in the valleys (see **Fig. 2**). Material parameters of several MX_2 , MX_Y , and substrate characteristics, used for FEM, are listed in **Table I**. All calculations were performed at room temperature $T = 300$ K.

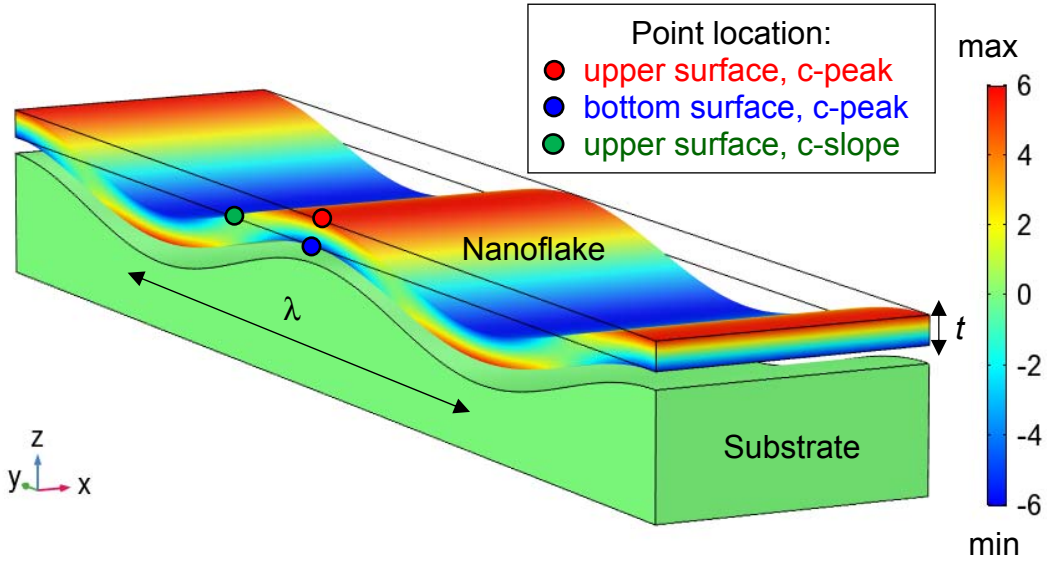


FIGURE 2. Considered geometry. A nanoflake of TMD is placed on a corrugated substrate. Right scale schematically shows the variation of electric polarization, induced by the flexoelectric effect, and electric conductivity, induced by inhomogeneous elastic strain via the deformation potential. The red and blue circles located at the upper and bottom surfaces of the nanoflake, which is placed at the peak of the substrate corrugation, are abbreviated as “**c-peak**”. The green circle located at the corrugation slope is abbreviated as “**c-slope**”. Further we analyze the behavior of the physical properties in these three characteristic points at the nanoflake surface.

The inhomogeneous elastic strain should induce the changes of the electron and hole charge density, $n(\vec{x})$ and $p(\vec{x})$, in the flake due to the coupling with band structure via a deformation potential:

$$\frac{n(\vec{x})}{n_0} = \frac{1}{n_0} \int_0^\infty \frac{g_n(\varepsilon)d\varepsilon}{1+\exp\left(\frac{\varepsilon-E_F+E_c+\Sigma_{ij}^e u_{ij}(\vec{x})-e\varphi}{k_B T}\right)} \sim \exp\left(-\frac{\Sigma_{ij}^e u_{ij}(\vec{x})-e\varphi}{k_B T}\right), \quad (4a)$$

$$\frac{p(\vec{x})}{p_0} = \frac{1}{p_0} \int_0^\infty \frac{g_p(\varepsilon)d\varepsilon}{1+\exp\left(\frac{-\varepsilon+E_F-E_v+\Sigma_{ij}^h u_{ij}(\vec{x})+e\varphi}{k_B T}\right)} \sim \exp\left(-\frac{\Sigma_{ij}^h u_{ij}(\vec{x})+e\varphi}{k_B T}\right), \quad (4b)$$

where $n_0 = \int_0^\infty \frac{g_n(\varepsilon)d\varepsilon}{1+\exp\left(\frac{\varepsilon-E_F+E_c}{k_B T}\right)}$ and $p_0 = \int_0^\infty \frac{g_p(\varepsilon)d\varepsilon}{1+\exp\left(\frac{-\varepsilon+E_F-E_v}{k_B T}\right)}$ are the electron and hole concentrations in the unstrained nanomaterial, $g_n(\varepsilon)$ and $g_p(\varepsilon)$ are the densities of electron and hole states, E_F is the Fermi energy, $k_B = 1.3807 \times 10^{-23}$ J/K is a Boltzmann constant, Σ_{ij}^e and Σ_{ij}^h are the deformation potential tensors for electrons and holes, respectively. The values $\Sigma_{ij}^{e,h}$ are the fitting parameters of the continuum model; they should be either taken from the first-principles calculations, or estimated from experiments. The values $\Sigma_{ij}^{e,h}$ are listed in **Table I** for several MX_2 . The proportionality in Eqs. (4) is valid for a Boltzmann-Planck-Nernst statistics of non-degenerated carriers. Since the band gap of MX_2 and MXY is about $(1 - 2)$ eV, we can expect that rippled MX_2 and MXY should become conductive, once the spontaneous strain value exceeds several %, which makes the product $|\Sigma_{ij}^{e,h} u_{ij}|$ much higher than the thermal energy $k_B T$.

Table I. Materials constants for a LD MX_2 and MXY , and rough substrate

Material	LD MoS_2	LD MoTe_2	LD or LS MoSTe
Symmetry/phase *	6/mmm, 2H or 1H	6/mmm, 2H or 1H	3m, 1H
Lattice constants (nm)	$c=1.1, a=0.32$	$c=1.4, a=0.35$	$c=1.3, a=b=0.34$
Elastic stiffness tensor (GPa)	$c_{11}=134.3, c_{12}=33.3$	$c_{11}=139.0, c_{12}=71.0$ (for $\nu>0$)	$c_{11}=116, c_{12}=28$
Young module E (GPa)	250 Ref.[53] 136 Ref.[54]	(90 – 110) Ref.[55] we use 100	105
Poisson ratio ν	-0.07 [56]	0.34 [55] (but $\nu=-0.08$ from [56])	0.24 – 0.30 [57]
Effective piezo-response tensor d_{ijk}^{eff} (pm/V)	$d_{11}^{eff} = 5.76$ [15] $d_{31}^{eff} = -0.018$ [15]	$d_{33}^{eff} \approx 3$ [24] $d_{11}^{eff} = 9.13$ [58] $d_{11}^{eff} = 7.39$ [27]	$d_{11}^{eff} = 5.1$ [57] $d_{31}^{eff} = 0.4$ [57]
surface-induced out-of-plane piezoelectric	$e_{31}^s = 0$ $e_{33}^s = 0$	$e_{31}^s = 0$ $e_{33}^s = 0$	$e_{31}^s = 50$ pC/m $ e_{33}^s < 5$ pC/m

coefficients e_{3jk}^s (pC/m)			[28, 33, 57]
Flexoelectric effect tensor f_{ijkl} (nC/m) Ref.[59]	$f_{13} = 4.44$ $f_{13} = 4.44$	$f_{13} = 9.50$ $f_{11} = 9.50$	unknown, set equal to $f_{13} = f_{33} = 6.47$
Deformation potential tensor Σ_{ij} (eV)	$\Sigma_h = 5.61$ [28] $\Sigma_e = -11.14$ [28] $\Sigma_g = -(13.8 - 17)$ Ref.[22]	$\Sigma_h = 4.2$ (this work) $\Sigma_e = -7$ (this work) $\Sigma_g = -(3.8 - 11)$ Ref.[22]	unknown, set equal to $\Sigma_h = -5$ (this work) $\Sigma_e = -7$ (this work)
Substrate characteristics	Adhesive stiffness varies in the range $S_A = (20 - 2)$ GPa, adhesion repulsive separation is equal to $\delta h_0 = 1.1$ nm. Substrate material is gold, graphite, mica and silica oxide. The average period of corrugation is $\lambda = 0.5 \mu\text{m}$, the amplitude A of substrate roughness varies from 0 to 11 nm. A substrate thickness (200 – 500) nm		

* We regard that LD MoX_2 is in the semiconducting H phase (typically 2H) under normal conditions. MXY monolayers lack the reflection symmetry and are neither 2H nor 1H [5].

III. CORRELATION BETWEEN POLAR AND ELECTRONIC PROPERTIES OF MX_2 AND MXY NANOFLLAKES

Spatial distributions and profiles of elastic strain, its gradient, polarization and charge density of the TMDs and JCs nanoflakes are shown in **Figs. 3-7**. Additional details are shown in **Figs. S2-S5** in **Appendix B** [52] and briefly described here. One period of the substrate corrugation profile $\vec{x}_s = \left\{0, 0, A \cos\left(\frac{2\pi}{\lambda} x_1\right)\right\}$ is shown in all these figures, and the unambiguous correlations between the maximal/minimal values of the strain, strain gradient, polarization and charge density are clearly seen at the corrugation period.

The cross-sections of the bending-induced elastic displacement, strain components, out-of-plane polarization, and carrier density distributions are shown in **Figs. 3a-3f** for MoS_2 , and in **Figs. 3g-3l** for MoTe_2 nanoflakes of the same thickness (~ 28 nm) on a thick rough substrate, respectively. It is seen that the nanoflake displacement, strain, strain gradient, out-of-plane polarization and charge density are modulated by the corrugation profile, being maximal at the corrugation peaks, zero at the slopes, and minimal in the valleys. At that the relative increase of the electron density for MoS_2 (more than 10 times) is much higher than that for a MoTe_2 (less than 5 times) [compare **Fig. 3f** and **3l**]. The regions enriched by holes (more than 10 times) exists in MoS_2 nanoflakes. Hence the appearance of the p-n junctions between the n-type and p-type regions are possible in MX_2 nanoflakes, similarly to the case of graphene-on-ferroelectric [11, 12]. The distinct feature of MX_2 nanoflakes-on-corrugated

substrate is that the width, diffuseness or sharpness of the p-n junctions can be controlled by the flake thickness t , and by the relative substrate corrugation, A/λ .

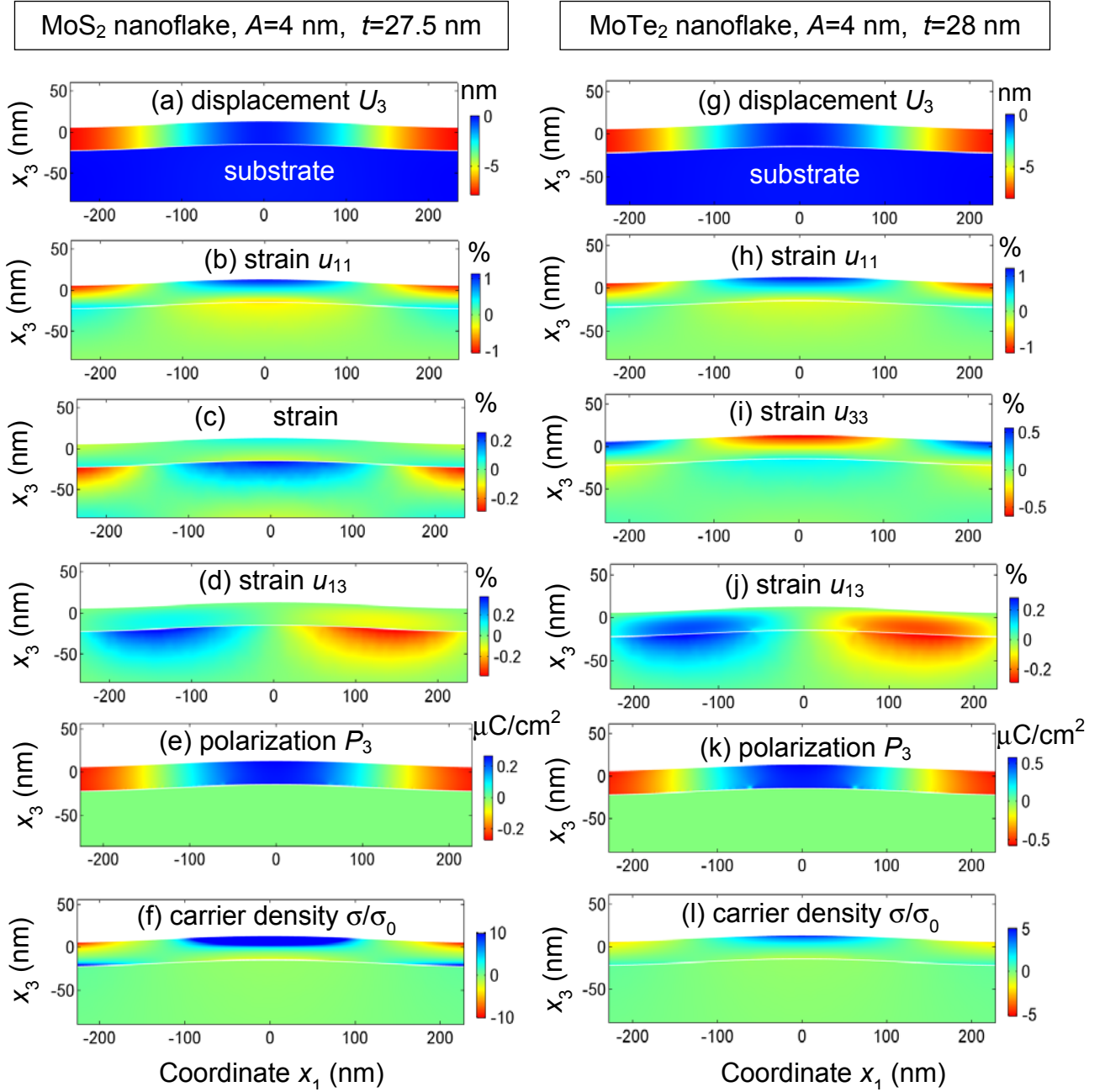


FIGURE 3. Distributions polar and electronic properties in MoS₂ (a-f) and MoTe₂ (g-l) nanoflakes. Bending-induced elastic displacement (**a**, **g**), strain tensor components (**b-d**, **h-j**), out-of-plane polarization (**e**, **k**), and relative static conductivity (**f**, **l**) in the cross-section of a MoS₂ (**a-f**) and MoTe₂ (**g-l**) nanoflake with thickness $t \approx 28$ nm, which is placed on a 200-nm thick rough substrate. The amplitude A of the substrate

corrugation is 4 nm, and the average period of the corrugation is $\lambda = 0.5 \mu\text{m}$. MoS₂, MoTe₂, and substrate parameters are listed in **Table I**.

The cross-sections of bending-induced elastic displacement, strain components, out-of-plane polarization for ultra-thin MoSTe nanoflakes (e.g. 10 layers or thinner, see **Figs. 4a-f**) looks only a bit different from thicker MX₂ nanoflakes (shown in **Figs. 3**) due to the thickness effect. When the MoSTe nanoflake thickness increases (see **Figs. 4a-f**), the overall picture looks as some “average” between the MoS₂ and MoTe₂ nanoflakes shown in **Figs. 3**. Note the possible appearance of the p-n junctions between the n-type and p-type regions in MXY nanoflakes, similarly to the case of MX₂ nanoflakes.

The influence of the surface-induced piezoelectric effect (present in MoSTe and absent for 1H and 2H-MoX₂) appears too small to affect significantly the polar and electronic properties distributions shown in **Fig. 4**. Hence even for the case of a JC MoSTe the dominant part of the polarization is the flexoelectric polarization. This conclusion is clearly seen from comparison of the scales in **Fig. S6a** and **S6b**, where the magnitude of the piezoelectric polarization is about 2 nC/cm², while the magnitude of the flexoelectric polarization is two orders higher – about 0.4 $\mu\text{C}/\text{cm}^2$ for the flake thickness $\sim (4 - 20)$ nm. At that the contribution of the surface-induced piezoelectric effect decreases with the flake thickness according to Eq.(3) (compare brown and black curves in **Fig. S6a**).

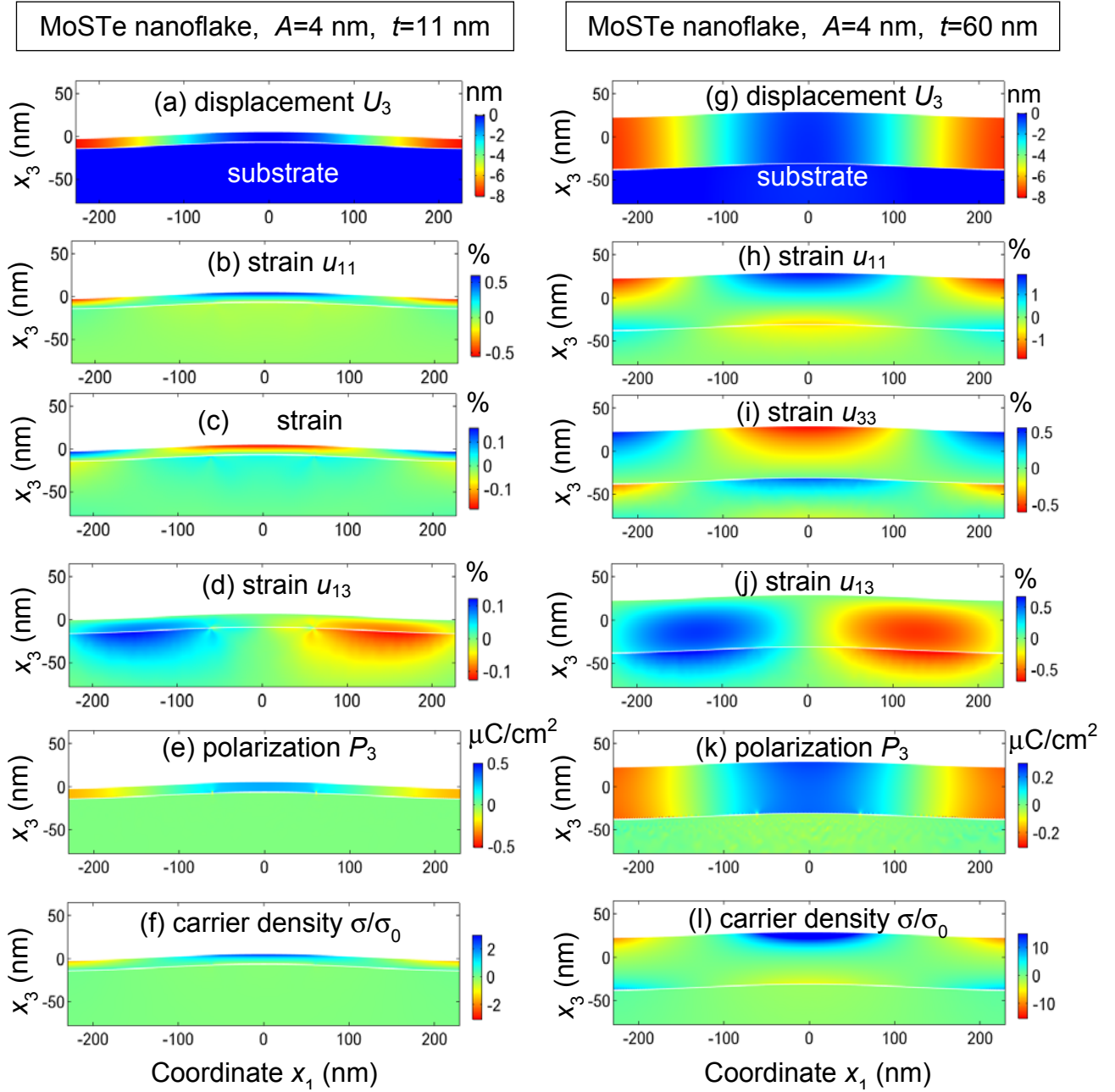


FIGURE 4. Distributions polar and electronic properties in MoSTe nanoflakes with thickness 11 nm (a-f) and 60 nm (g-l). Bending-induced elastic displacement (a,g), strain tensor components (b-d, h-j), out-of-plane polarization (e,k), and relative static conductivity (f,l) in the cross-section of the nanoflake placed on a thick rough substrate. The amplitude A of the substrate corrugation is 4 nm, and the average period of the corrugation is $\lambda = 0.5 \mu\text{m}$. MoSTe and substrate parameters are listed in **Table I**.

The curves in **Fig. 5** are calculated for different amplitudes of substrate roughness $A = (0 - 11)\text{nm}$ and approximately the same thickness $\sim 11 \text{ nm}$ (corresponding to the range from 10 to 8

layers) of MoS₂, MoTe₂ and MoSTe nanoflakes. The bending-induced out-of-plane flexoelectric polarization and relative electron density monotonically increase with A increase. At that the relative increase of the electron density for MoS₂ ($>10^3$ times) is much higher than that for a MoTe₂ (>10 times), and also than that for a MoSTe (>20 times), compare **Fig. 5b, 5d** and **5f**. The difference is related with significantly higher electronic deformation potential of MoS₂ (see **Table I**). The profiles of the out-of-plane flexoelectric polarization, which is proportional to the strain gradient, demonstrate visible deviations from the sinusoidal profile of substrate, since the top regions of the 10 curves plotted for $A = (2 - 11)$ nm have two symmetric indentations, which height increases and location becomes closer to the peak $x_1 = 0$ with A increase (see **Fig. 5a, 5c** and **5e**).

Bending dependence of polar and electronic properties of MoS₂ and MoTe₂ nanoflakes are shown in **Fig. 6a-b** and **6c-d**, respectively. The bending-induced elastic strain and strain gradient, out-of-plane flexoelectric polarization and relative electron density of the nanoflakes monotonically increase with the increase of corrugation amplitude A . The increase of the strain and electron density is linear at small $A < 5$ nm and becomes super-linear at $A > 10$ nm; it is much higher at the upper surface of the nanoflake in comparison with its bottom surface (compare red/brown and blue/black circles in **Fig. 6a** and **6d**). In contrast, the strain gradient and flexoelectric polarization, which increase linearly with the amplitude A increase, are almost the same at the upper and bottom surfaces (compare red/brown and blue/black circles in **Fig. 6b** and **6c**). Note the qualitative similarity, but the quantitative difference between MoS₂ and MoTe₂ nanoflakes, which are the most pronounced for polarization ($2 \mu\text{C}/\text{cm}^2$ vs. $4 \mu\text{C}/\text{cm}^2$), and relative electron density ($\gg 10^3$ vs. 10^2) maximal values.

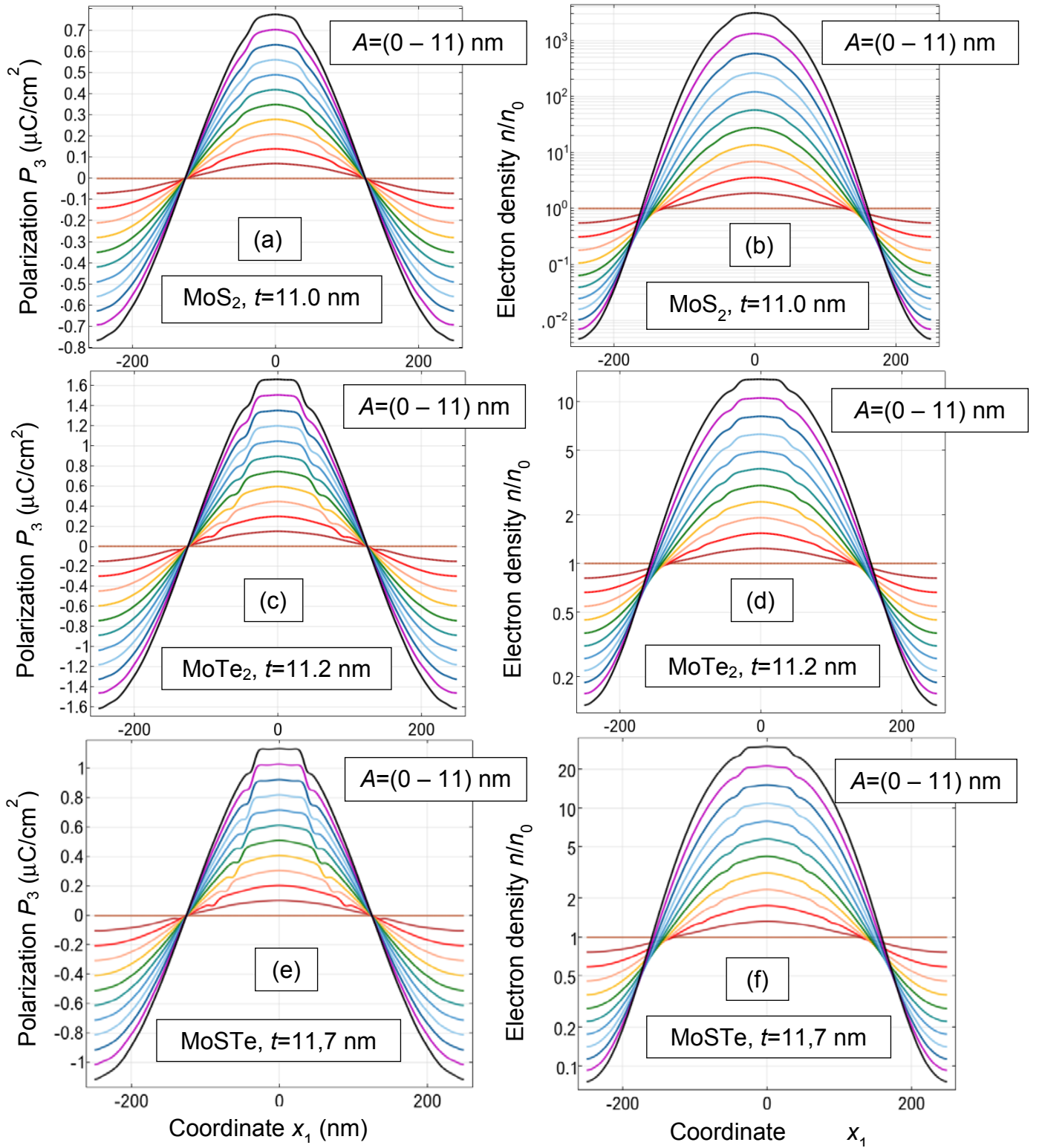


FIGURE 5. Profiles of polar and electronic properties of MoS₂, MoTe₂ and MoSTe nanoflakes. Bending-induced out-of-plane polarization (a, c, e), and relative electron density (b, d, f) at the upper surface of the nanoflake with thickness $t \approx 11$ nm, which is placed on a thick rough substrate. Twelve curves (from “0” brown

line to the top black curve) correspond to the different values of corrugation amplitude $A = 0, 1, 2, 3, 4, \dots, 11$ nm. Nanoflakes and substrate parameters are listed in **Table I**.

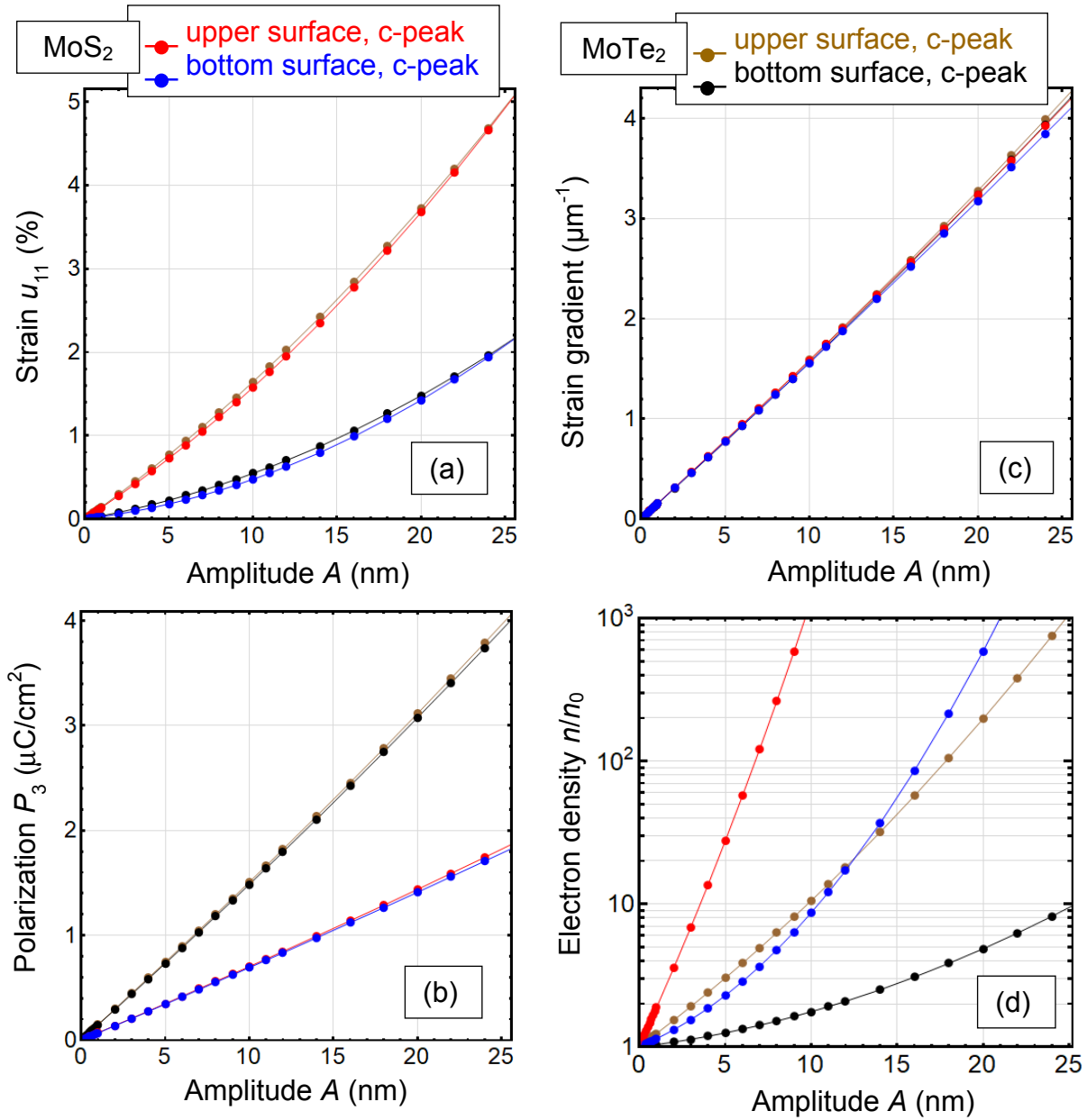


FIGURE 6. Bending dependence of polar and electronic properties of MoS₂ (red and blue circles) and MoTe₂ (brown and black circles) nanoflakes. The bending-induced elastic strain (a) and strain gradient (b), out-of-plane polarization (c) and relative electron density (d) of a nanoflake via the corrugation amplitude A of the rough substrate. The quantities (a)-(d) are shown at the upper (red and brown circles) and bottom (blue and black circles) surfaces of the nanoflake, which are placed at the peaks of the substrate corrugation (abbreviated

as “c-peak”, see **Fig. 2**). The flake thickness is 11 nm, the average period of corrugation $\lambda = 0.5 \mu\text{m}$. MoX_2 and substrate parameters are listed in **Table I**.

Thickness dependence of polar and electronic properties of MoS_2 and MoTe_2 nanoflakes are shown in **Fig. 7**. Blue/black and red/brown circles, which correspond to the corrugation peaks, where the strain and strain gradient are maximal, show the maximal increase of the flexoelectric polarization, electron or hole densities. Green/purple circles, which correspond to the corrugation slope, where the strain and strain gradient are absent, show almost zero polarization and no increase in the electron or hole density. Most important that there is a pronounced maximum at the thickness dependences of the elastic strain, electron and hole conductivity of MoS_2 and MoTe_2 nanoflakes placed on a rough substrate. The optimal thickness is corrugation dependent, and it is 75 nm for MoS_2 and 80 nm MoTe_2 nanoflakes for the case of 4 nm corrugation height. The result opens the way for the geometry optimization of nanoflake placed on a substrate with a sinusoidal corrugation profile.

Note, that corresponding bending and thickness dependence curves for MoSTe nanoflakes lay between MoS_2 and MoTe_2 nanoflakes, as anticipated from **Fig. 5**. They are not shown in **Figs. 6** and **7**, since the “mixture of curves” appears when we add two or three more curves.

Analysis of the above FEM results obtained for the different flake thickness (varying from 10 to 300 nm) and corrugation depth (varying from 0 to 25 nm), allows to corroborate the flexoelectric nature of the out-of-plane polarization [24] and establish the unambiguous correlation between the polarization and *n*-type (or *p*-type) static conductivity modulation. The modulation is caused by inhomogeneous elastic strains coupled with deformation potential, and strain gradients, which evolve in TMD nanoflake due to the adhesion between the flake surface and corrugated substrate.

Obtained results can be useful for elaboration of nanoscale straintronic devices based on the MX_2 and MXY nanoflakes bended by a corrugated substrate. Principal schemes of diodes and bipolar transistors are presented in **Fig. 8**, where the bending profile of a semiconducting nanoflake controls the sharpness of p-n junctions between the regions with *n*-type (electron) and *p*-type (hole) conductivity. To create real prototypes of devices, one should take into account possible disadvantages related with a "doubled" geometry of the obtained p-n junctions. Namely we calculated more faint “extra” p-regions located at the flake-substrate boundary below the top *n*-regions, and “extra” *n*-regions located at the flake-substrate boundary below the top *p*-regions. However, for a specific device architecture the “doubled” geometry in complex with very high mechanical stability and flexibility of the nanoflakes-on-substrate may become a benefit.

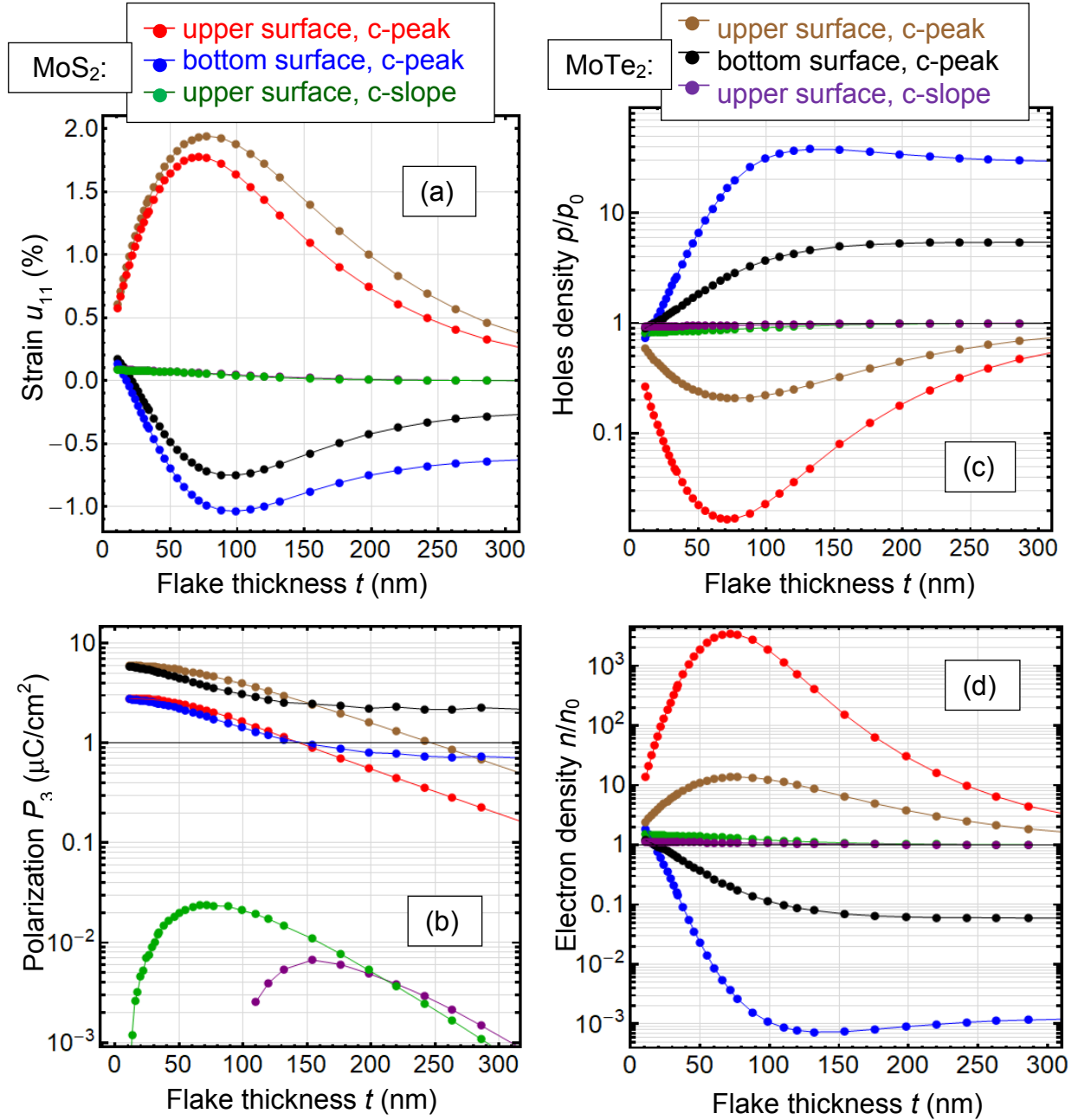


FIGURE 7. Thickness dependence of polar and electronic properties of MoS₂ (red, green and blue circles) and MoTe₂ (brown, purple and black circles) nanoflakes. The bending-induced elastic strain (a), out-of-plane polarization (b), hole (c), and (d) electron densities via the thickness of a nanoflake placed on a rough substrate. The quantities (a)-(d) are shown at the upper (red and brown circles) and bottom (blue and black circles) surfaces of the nanoflake, which are placed at the peaks of the substrate corrugation (abbreviated as “c-peak”, see Fig. 2). Green and purple circles correspond to the corrugation slope (abbreviated as “c-slope”, see Fig. 2). The amplitude of substrate corrugation $A = 4$ nm, the average period of the corrugation $\lambda = 0.5$ μm . MoX₂ and substrate parameters are listed in **Table I**.

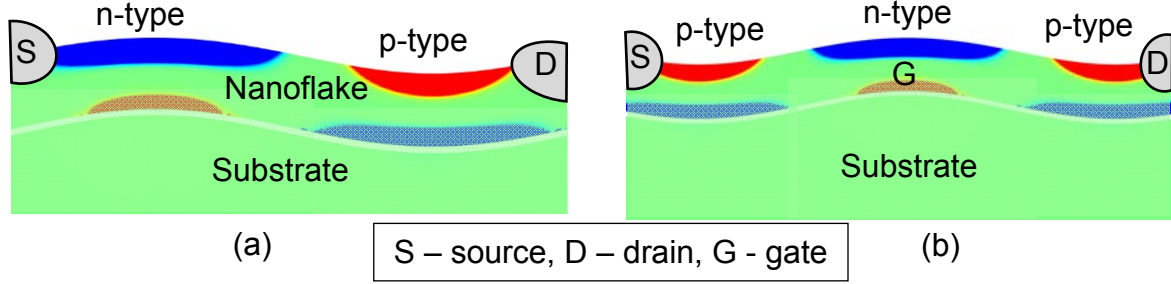


FIGURE 8. Principal schemes of a diode **(a)** and bipolar transistor **(b)** based on a 13 nm thick MoSTe nanoflake bended by a corrugated substrate. The regions with n-type (electron) and p-type (hole) conductivity are shown.

To resume the section, the considered 2D problem can describe quantitatively the real situation when a nanoflake is placed on a highly-oriented substrate with almost perfect 1D corrugation profile obtained by e.g., self-assembling or self-organization. For the case we expect that it is possible to reach high conductivity, which is strongly correlated with relatively high flexoelectric polarization, by selecting the optimal ratio between the corrugation period λ , its amplitude A and nanoflake thickness t .

However, the real ripples cannot be completely 1D, and the corrugation in other directions can be present also. FEM for the case of a substrate with 2D corrugation profile (and especially with random 3D corrugation profile) is a significantly more complex task requiring much more computer time and memory resources, which increase with the flake thickness. Our preliminary FEM results confirm the strong correlation between the enhanced conductivity of the nanoflake and its flexoelectric polarization at the corrugation peaks. The enhancement is more pronounced for higher ratio $\frac{\text{pick height}}{\text{pick width}}$ that is an analog of $\frac{A}{\lambda}$ ratio in 1D case, but the effect of carrier density inversion at the valleys is rather weak or non-observable. This is related with the strain concentration at the localized corrugation peaks and their relaxation in the valleys.

In overall, FEM results for 2D and 3D corrugated substrates are not obvious and require a separate study. Moreover, due to the effect complexity for the most realistic case of the substrate with a random 3D corrugation, the procedure of the nanoflakes polar and conductive properties optimization will be much more complex in comparison with the flakes on 1D-corrugated substrates considered in this work.

IV. COMPARISON WITH EXPERIMENT

Note that the calculated strain-induced enhancement of carrier density is regulated by the components Σ_{ij} of deformation potential tensor, which are fitting parameter within the continuum media approach used in FEM. An appropriate choice of the Σ_{ij} (either from DFT calculations or from experiment) can lead to the enhancement in $5 - 10^4$ times. This tunability makes FEM complementary to the Duerloo et. al. [60] results, who predicted a strain-induced phase transition from a semiconducting 2H to a metallic 1T' phase in various MX_2 . Later on, and Song et. al. [61] observed a room temperature semiconductor–metal transition in thin MoTe_2 films induced by a homogeneous tensile strain of 0.2%.

Our FEM results, obtained for the case of inhomogeneous periodic bending of MX_2 nanoflakes, better agrees with Kang et. al. experiment [24], who establish the correlations between AFM topography and C-AFM conductive spots in MoTe_2 nanoflakes placed on a gold corrugated substrate. Kang et. al. observed multiple conductive spots located at the corrugation peaks (see e.g. parts (a,b) and (e) in fig. S5 in the Supplement to Ref.[24]). The difference in the negative C-AFM contrast at the corrugation peaks (-15 nA) in comparison to positive C-AFM contrast at the valleys (+4 nA) was about 4.75 times, that is very close to the ratio of maximal/minimal carrier density (about 5 times) shown in **Fig. 3I** and **Fig. 9**.

Figure 9 compares the experimental results [24] and FEM results obtained in this work. The left side of the figure shows the surface topography (top image) and C-AFM contrast (bottom image) of MoTe_2 nanoflake with thickness 10 nm measured by Kang et al [24]. The right side shows the corrugation (top image) and relative carrier density σ/σ_0 (bottom image) color maps calculated by FEM for a 10 nm thick MoTe_2 nanoflake placed on a rough substrate with several well-separated corrugation peaks. We regarded that each peak has a Gaussian distribution of corrugation with its own height, maximum position and dispersion, which values are random, but have the same order as in the experiment [24]. Assuming that the carrier density is proportional to C-AFM contrast in the simplest case, **Fig. 9** demonstrates a semi-quantitative agreement between our simulations and experiment [24]. Notably that both experimentally measured topography peaks and calculated corrugation distribution look much more diffuse and often merging together in comparison with a well-separated measured C-AFM contrast and calculated carrier density spots. Since the carrier density $\sigma(\vec{x})$ exponentially depends on the flake strain $u_{ij}(\vec{x})$ in accordance with Eqs.(4), $\frac{\sigma(\vec{x})}{\sigma_0} \sim \exp\left(-\frac{\Sigma_{ij}u_{ij}(\vec{x})}{k_B T}\right)$, and the flake strain is rather linear function of the substrate corrugation, the carrier density should be a sharp (e.g.,

exponential) function of the corrugation. So, we can conclude that our simulations confirm the fact that the enhancement of local carrier density (and so the local conductivity) is pronounced at the corrugation peaks, but the effect of the carrier density inversion at the valleys and slopes is relatively weak. This is related with the strain concentration at the corrugation peaks and their relaxation in the valleys. The enhancement at the peaks is inherent for a 3D problem, while 1D-corrugation can lead to the inversion effect in the valleys (compare **Figs. 3** and **9**).

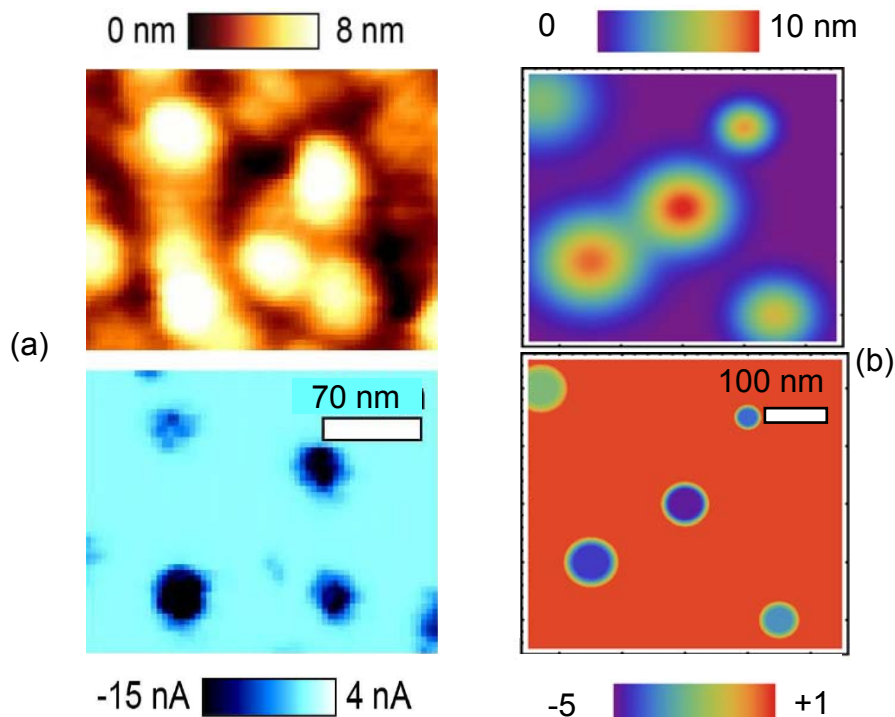


Figure 9. (a) Surface topography (top image) and C-AFM contrast (bottom image) of a 10 nm thick MoTe₂ nanoflake obtained for the *dc* voltage -0.25 V applied to the tip. Reprinted with permission from [S. Kang, S. Jeon, S. Kim, D. Seol, H. Yang, J. Lee, Y. Kim, ACS Appl. Mater. Interfaces 10 (2018) 27424-27431]. Copyright (2018) ACS Publications. (b) Corrugation (top image) and relative carrier density σ/σ_0 (bottom image) color maps calculated by FEM for a 10 nm thick MoTe₂ nanoflake placed on a rough substrate with several well-separated corrugation peaks.

To verify theoretical results for MoS₂ nanoflakes, their structure was examined by a scanning tunneling microscopy (STM) in non-vacuum conditions (see details in **Appendix C** [52]). As substrates we used highly-ordered pyrolytic graphite (HOPG) and Au(111) on mica. STM images, shown in **Fig. S7 – S8**, revealed MoS₂ nanoflakes of different shape and size. Typical local volt-

ampere characteristics (I-V curves) measured at the same point of a nanoflake are shown in **Fig. 10** (more I-V curves are shown in **Fig. S7 – S8**).

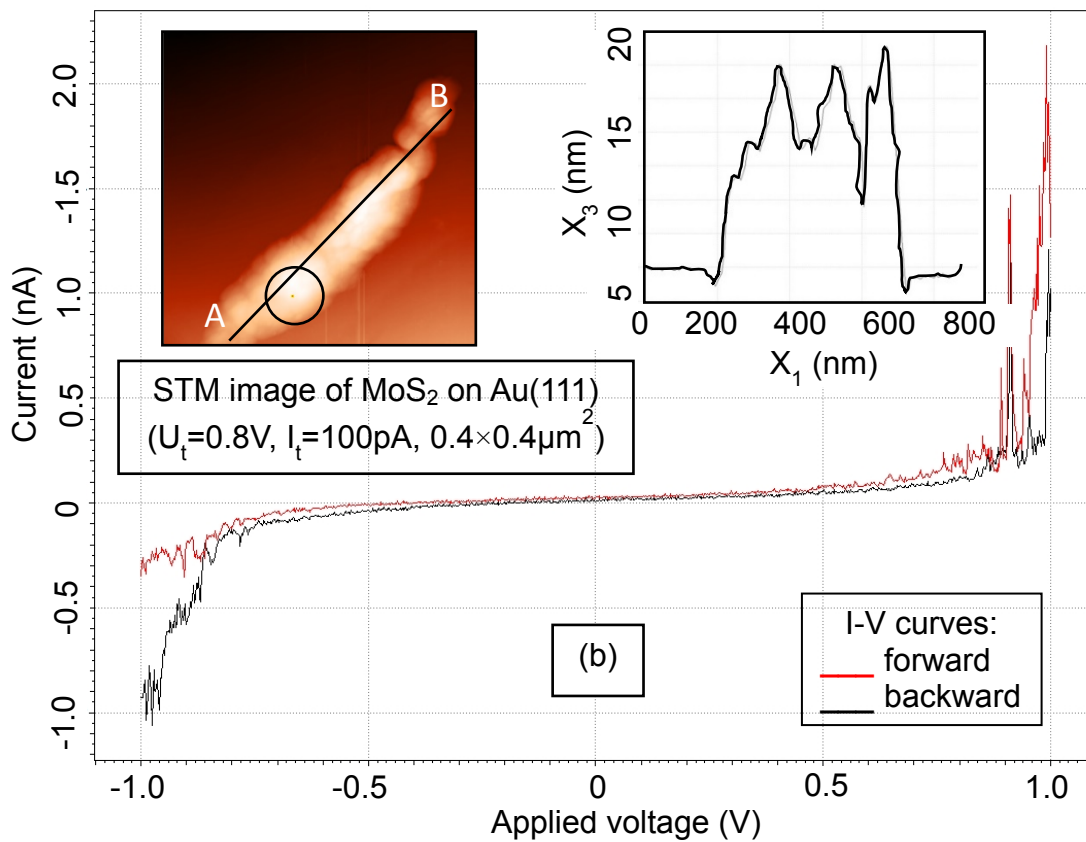
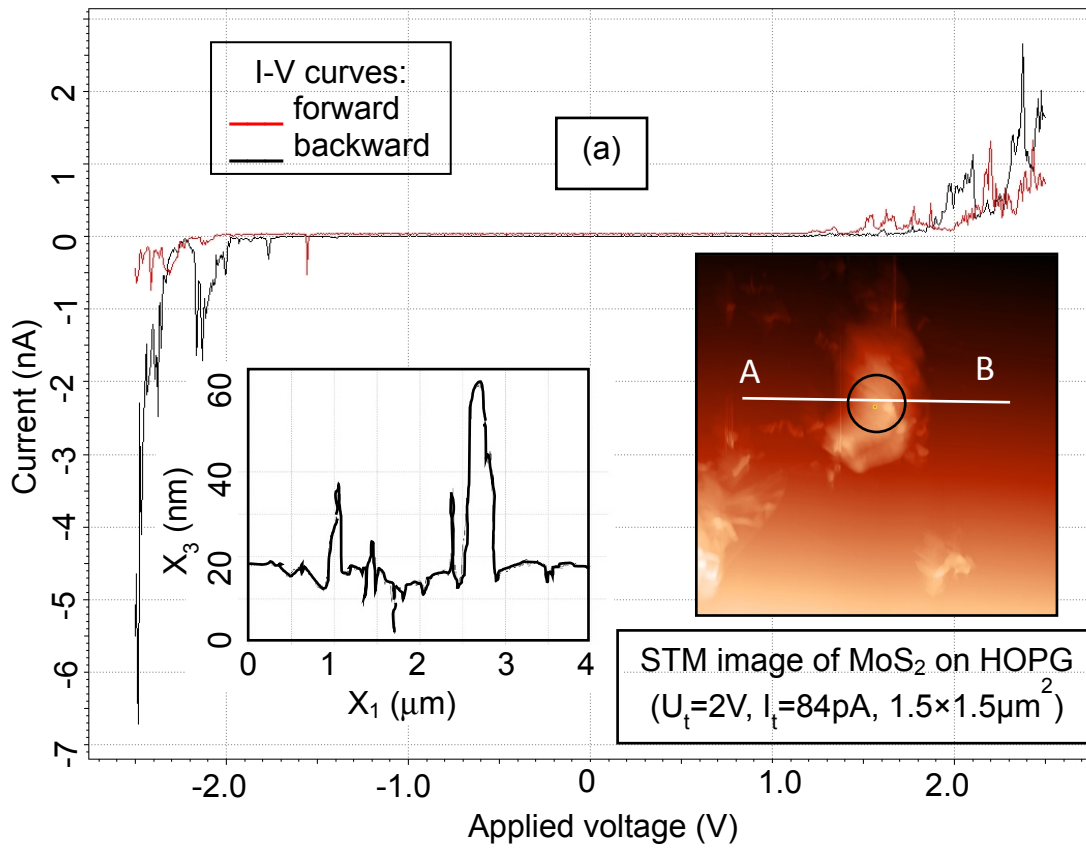


Figure 10. Local volt-ampere characteristics of MoS₂ nanoflakes on **(a)** HOPG and **(b)** Au(111) substrates measured by STM. Left inset in the plot (a) and right inset in the plot (b) are the surface topography along the direction AB. Right inset in the plot (a) and left inset in the plot (b) are the STM images of MoS₂ nanoflakes on HOPG and Au(111) substrates, respectively. Local volt-ampere characteristics were measured in the points marked by a circle with a central yellow-red rectangle in the insets.

The tunneling current is almost absent if the voltage magnitude is less than 1 V for HOPG substrate or less than 0.5 V for Au(111) substrate. The difference in the “opening” voltages of the I-V curves originates from the difference of substrate conductivity and surface properties. Since both substrates do not contain any specially prepared corrugations, the current is absent for a strain-free nanoflake placed in a small electric field. A strong local field appearing under the bias voltage increase causes the flake local bending and deformation due to the electrostriction and piezoelectric mechanisms. At that the strained region of the flake can become conductive and lead to the “opening” of the I-V curve.

The significant variability of the I–V curves opening scenario and typical jumps on the curves, which appear at applied voltage magnitude more than (0.5 – 1)V, indicate the randomness of a tunneling current path associated with the strong local inhomogeneity of electroconductivity near the surface of MoS₂ nanoflakes, which is most likely caused by the shape changes of the nanoflakes and by the evolution of local electric fields under the current flow. In fact, the strong local inhomogeneity of the MoS₂ nanoflake conductivity can be determined by the bending of its surface in accordance with FEM results presented in this work. Hence STM results indirectly indicates a significant dependence of free carrier concentration in MoS₂ nanoflakes on their bending and strain gradient. The quantitative description of these results requires theoretical calculations of local electric fields coupled to elastic strains for different substrates and nanoflake shape/sizes. This task will be performed in near future.

V. SUMMARY

Using FEM, we calculated the elastic and electric fields, out-of-plane electric polarization and free charge density for a TMD nanoflake placed on a rough substrate with a sinusoidal profile of the corrugation principal component. Analysis of FEM results obtained for the different flake thickness (varying from 10 to 300 nm) and corrugation depth (varying from 0 to 25 nm), allows to corroborate the flexoelectric nature of the out-of-plane polarization and establish the unambiguous correlation between the polarization and static conductivity modulation. We regarded that the modulation is caused by inhomogeneous elastic strains coupled with deformation potential, and strain gradients,

which evolve in the TMD nanoflake due to the adhesion between the flake surface and the corrugated substrate.

We revealed a pronounced maximum at the thickness dependences of the electron and hole conductivity of MoX_2 and MXY nanoflakes placed on a substrate with a sinusoidal corrugation. Namely the conductivity is maximal for a (75 – 80) nm thick flakes placed on a rough substrate with the 4 nm corrugation height. This result opens the way for the nanoflakes geometry optimization towards significant improvement their polar and electronic properties, necessary for their advanced applications in nanoelectronics and memory devices. Specifically, obtained results can be useful for elaboration of nanoscale straintronic devices based on the bended MX_2 and MXY nanoflakes, such as diodes and bipolar transistors with a bending-controllable width of p-n junctions.

Acknowledgements. This effort (S.V.K.) is based upon work supported by the US Department of Energy (DOE), Office of Science, Basic Energy Sciences (BES), Materials Sciences and Engineering Division and was performed at the Oak Ridge National Laboratory's Center for Nanophase Materials Sciences (CNMS), a US Department of Energy, Office of Science User Facility. This work (Y.K.) was supported by the Basic Science Research Program through the National Research Foundation of Korea (NRF) funded by the Ministry of Education (No. 2019R1A6A1A03033215). A.N.M, H.V.S., Y.Y.L. and G.I.D. work has received funding from the National Research Foundation of Ukraine (Grant application 2020.02/0027). A.N.M., Y.Y.L. and G.I.D. acknowledges multiple stimulating discussions with Prof. A.A. Marchenko (IP NASU).

Authors' contribution. A.N.M., Y.K. and S.V.K. generated the research idea. A.N.M evolved the theoretical model, state the problem, interpreted numerical results obtained by E.A.E. and H.V.S., and jointly with Y.K. and S.V.K. wrote the manuscript draft. Y.Y.L. performed STM measurements. G.I.D., Y.K. and S.V.K. worked on the results discussion and manuscript improvement.

REFERENCES

-
- ¹ S. Kang, S. Kim, S. Jeon, W.-S. Jang, D. Seol, Y.-M. Kim, J. Lee, H. Yang, and Y. Kim. Atomic-scale symmetry breaking for out-of-plane piezoelectricity in two-dimensional transition metal dichalcogenides. *Nano Energy* **58**, 57 (2019).
- ² R. Grasset, Y. Gallais, A. Sacuto, M. Cazayous, S. Mañas-Valero, E. Coronado, and M.-A. Méasson. Pressure-induced collapse of the charge density wave and higgs mode visibility in 2 H- TaS 2. *Phys. Rev. Lett.* **122**, 127001 (2019).
- ³ C.J. Butler, H.-H. Yang, J.-Y. Hong, S.-H. Hsu, R. Sankar, C.-I. Lu, H.-Y. Lu, K.-H.O. Yang, H.-W. Shiu, C.-H. Chen, C.-C. Kaun, G.-J. Shu, F.-C. Chou and M.-T. Lin. Mapping polarization induced surface band bending on the Rashba semiconductor BiTeI. *Nat. Commun.* **5**, Article number: 4066 (2014).
- ⁴ Y. Qi, W. Shi, P.G. Naumov, N. Kumar, R. Sankar, W. Schnelle, C. Shekhar, Fang C. Chou, C. Felser, B. Yan, S.A. Medvedev, Topological quantum phase transition and superconductivity induced by pressure in the bismuth tellurohalide BiTeI. *Advanced Materials* **29**, 1605965 (2017).
- ⁵ L. Dong, J. Lou, and V.B. Shenoy. Large in-plane and vertical piezoelectricity in Janus transition metal dichalcogenides. *ACS nano* **11**, 8242 (2017).
- ⁶ E. A. Eliseev, A. N. Morozovska, and M. V. Strikha. Strain engineering of ferromagnetic-graphene-ferroelectric nanostructures. *Phys. Rev. Applied* **14**, 024081 (2020)
- ⁷ A.A. Bukharaev, A. Zvezdin, A. Pyatakov, Yu. Fetisov. Straintronics: a new trend in micro-, nanoelectronics, and material science. *Physics-Uspekhi*, **61**, 1175 (2018).
- ⁸ G. Catalan, J. Seidel, R. Ramesh, and J. F. Scott. Domain wall nanoelectronics. *Rev. Mod. Phys.* **84**, 119 (2012).
- ⁹ A.P. Pyatakov, A. K. Zvezdin. Magnetoelectric and multiferroic media. *Phys. Usp.* **52**, 557 (2012); *Usp. Fiz. Nauk*, **182**, 593 (2012).
- ¹⁰ D. Sando, A. Agbelele, D. Rahmedov, J. Liu, P. Rovillain, C. Toulouse, I. C. Infante, A. P. Pyatakov, S. Fusil, E. Jacquet, C. Carrétéro, C. Deranlot, S. Lisenkov, D. Wang, J-M. Le Breton, M. Cazayous, A. Sacuto, J. Juraszek, A. K. Zvezdin, L. Bellaiche, B. Dkhil, A. Barthélémy, and M. Bibes. Crafting the magnonic and spintronic response of BiFeO₃ films by epitaxial strain. *Nature Materials* **12**, 641 (2013).
- ¹¹ A. I. Kurchak, E. A. Eliseev, S. V. Kalinin, M. V. Strikha, and A. N. Morozovska. P-N junctions dynamics in graphene channel induced by ferroelectric domains motion. *Phys. Rev. Applied* **8**, 024027 (2017)

-
- ¹² A. I. Kurchak, A. N. Morozovska, E. A. Eliseev, S. V. Kalinin and M. V. Strikha. Nontrivial temperature behavior of the carrier concentration in the nanostructure "graphene channel on ferroelectric substrate with domain walls". *Acta Materialia* **155**, 302 (2018)
- ¹³ W. Wu, L. Wang, Y. Li, F. Zhang, L. Lin, S. Niu, D. Chenet, X. Zhang, Y. Hao, T.F. Heinz, J. Hone, and Z.L. Wang, Piezoelectricity of single-atomic-layer MoS₂ for energy conversion and piezotronics. *Nature* **514**, 470 (2014).
- ¹⁴ S. Yuan, X. Luo, H.L. Chan, C. Xiao, Y. Dai, M. Xie, and J. Hao. Room-temperature ferroelectricity in MoTe₂ down to the atomic monolayer limit. *Nat. Commun.* **10**, 1775 (2019).
- ¹⁵ J.H. Choi, S.H. Jhi. Origin of robust out-of-plane ferroelectricity in 1T-MoS₂ monolayer. *J.Phys.: Cond. Matt.* **32**, 045702 (2020).
- ¹⁶ K.-A.N. Duerloo, Y. Li, and E.J. Reed, Structural phase transitions in two-dimensional Mo- and W-dichalcogenide monolayers, *Nat. Commun.* **5**, 4214 (2014).
- ¹⁷ A.N. Enyashin, L. Yadgarov, L. Houben, I. Popov, M. Weidenbach, R. Tenne, M. Bar-Sadan, and G. Seifert. New route for stabilization of 1T-WS₂ and MoS₂ phases. *J. Phys. Chem. C* **115**, 24586 (2011).
- ¹⁸ G. Eda, T. Fujita, H. Yamaguchi, D. Voiry, D. Chen, M. Chhowalla, Coherent Atomic and Electronic Heterostructures of Single-Layer MoS₂. *ACS Nano* **6**, 7311 (2012).
- ¹⁹ J. Suh, T.L. Tan, W. Zhao, J. Park, D.-Y. Lin, T.-E. Park, J. Kim. Reconfiguring crystal and electronic structures of MoS₂ by substitutional doping. *Nat. Comm.* **9**, article number: 199 (2018).
- ²⁰ D.W. Boukhvalov and M.I. Katsnelson. Enhancement of chemical activity in corrugated graphene. *J. Phys. Chem. C* **113**, 14176 (2009).
- ²¹ S.V. Kalinin, and V. Meunier. Electronic flexoelectricity in low-dimensional systems. *Phys. Rev. B*, **77**, 033403 (2008).
- ²² P. Johari, and V.B. Shenoy. Tuning the electronic properties of semiconducting transition metal dichalcogenides by applying mechanical strains. *ACS nano* **6**, 5449 (2012).
- ²³ J. Berry, S. Zhou, J. Han, D.J. Srolovitz, and M.P. Haataja. Domain morphology and mechanics of the H/T' transition metal dichalcogenide monolayers. *Phys. Rev. Mater.* **2**, 114002 (2018).
- ²⁴ S. Kang, S. Jeon, S. Kim, D. Seol, H. Yang, J. Lee, and Y. Kim. Tunable out-of-plane piezoelectricity in thin-layered MoTe₂ by surface corrugation-mediated flexoelectricity. *ACS Appl. Mater. Inter.* **10**, 27424 (2018).
- ²⁵ J. Berry, S. Zhou, J. Han, D.J. Srolovitz, and M.P. Haataja. Dynamic phase engineering of bendable transition metal dichalcogenide monolayers. *Nano Letters* **17**, 2473 (2017).

-
- ²⁶ H. Zhu, Y. Wang, J. Xiao, M. Liu, S. Xiong, Z.J. Wong, Z. Ye, Y. Ye, X. Yin and X. Zhang, Observation of piezoelectricity in free-standing monolayer MoS₂. *Nat. Nanotechnol.* **10**, 151 (2015).
- ²⁷ M.B. Ghasemian, T. Daeneke, Z. Shahrabaki, J. Yang, and K. Kalantar-Zadeh. Peculiar piezoelectricity of atomically thin planar structures. *Nanoscale* 12, 2875 (2020).
- ²⁸ W.-Z. Xiao, H.-J. Luo, and L. Xu. Elasticity, piezoelectricity, and mobility in two-dimensional BiTeI from a first-principles study. *J. Phys. D: Appl. Phys.* 53, 245301 (2020).
- ²⁹ T. Dumitrica, C.M. Landis, B.I. Yakobson, Curvature-induced polarization in carbon nanoshells, *Chem. Phys. Lett.* **360**, 182 (2002).
- ³⁰ I. Naumov, A.M. Bratkovsky, and V. Ranjan. Unusual Flexoelectric Effect in Two-Dimensional Noncentrosymmetric sp²-Bonded Crystals. *Phys. Rev. Lett.* 102, 217601 (2009).
- ³¹ W. Shi, Y. Guo, Z. Zhang, and W. Guo, Flexoelectricity in Monolayer Transition Metal Dichalcogenides, *J. Phys. Chem. Lett.* 9, 6841 (2018).
- ³² The adjectives “in-plane” and “out-of-plane” are used here to describe the polarization direction parallel or perpendicular to the surface of a thin film (see e.g. [N. Setter, D. Damjanovic, L. Eng, G. Fox, Spartak Gevorgian, S. Hong, A. Kingon et al. "Ferroelectric thin films: Review of materials, properties, and applications. *J. Appl. Phys.*100, 051606 (2006)]
- ³³ M.N. Blonsky, H.L. Zhuang, A.K. Singh, and R.G. Hennig. Ab initio prediction of piezoelectricity in two-dimensional materials. *ACS Nano* 9, 9885 (2015).
- ³⁴ M.M. Alyoꝛuꝛk, Y. Aierken, D. Cꝛakır, F.M. Peeters, and C. Sevik. Promising piezoelectric performance of single layer transition-metal dichalcogenides and dioxides. *J. Phys. Chem. C* 119, 23231 (2015).
- ³⁵ A.N. Morozovska, E.A. Eliseev, K.D. Stubbs, R. Vasudevan, Y.Kim, and S.V. Kalinin. Phase Diagrams of Single Layer Two-Dimensional Transition Metal Dichalcogenides: Landau Theory. *Phys. Rev. B*, 101, 195424 (2020).
- ³⁶ A.N. Morozovska, E.A. Eliseev, G.I. Dovbeshko, M.D. Glinchuk, Y. Kim, and S.V. Kalinin. Flexo-induced ferroelectricity in low dimensional transition metal dichalcogenides. *Phys. Rev. B* **102**, 075417 (2020).
- ³⁷ G.I. Dovbeshko. Surface Enhanced IR Absorption of Nucleic Acids from Tumor Cells: FTIR Reflectance Study. *Biopolymers (Biospectroscopy)* 67, 470 (2002).
- ³⁸ The “effective” force matrix F_{ij}^A is used in the context describing interatomic forces acting between different ions in the harmonic approximation. For a given ion A the matrix consists of the second spatial derivatives of the effective potential $U_A(x_1, x_2, x_3)$ of the ion, $F_{ij}^A = \frac{\partial^2 U_A}{\partial x_i \partial x_j}$ (see e.g. the textbooks [Ch. Kittel, Introduction to

solid state physics, London, Chapman & Hall (1956)], [A.I. Anselm, Introduction to semiconductor theory. Mir, Moscow, Prentice-Hall, Englewood Cliffs, NJ, 1981]).

³⁹ K.T. Kang, J. Park, D. Suh, and W.S. Choi, Synergetic Behavior in 2D Layered Material/Complex Oxide Heterostructures, *Advanced Materials*, **31**, 1803732 (2019).

⁴⁰ T.F. Kuech, Integration of Dissimilar Materials, *in* Comprehensive Semiconductor Science and Technology, vol. 4, edited by P. Bhattacharya, R. Fornari and H. Kamimura (Elsevier Science, 2011).
<https://www.sciencedirect.com/topics/chemistry/van-der-waals-force>

⁴¹ M. Inoue, Structural integrity of metal–polymer adhesive interfaces in microelectronics, *Chapter 6 in* Advanced Adhesives in Electronics, edited by M.O. Alam and C. Bailey (Woodhead Publishing, 2011).

⁴² S.P. Koenig, N.G. Boddeti, M.L. Dunn, and J.S. Bunch. Ultrastrong adhesion of graphene membranes. *Nature Nanotechnology* **6**, 543 (2011).

⁴³ X. Zhaoa, M. Boaa, Z. Huangb, J. Zhoua, C. Penga, L. Li. Heterojunction bond relaxation and electronic reconfiguration of WS₂- and MoS₂-based 2D materials using BOLS and DFT. *Applied Surface Science* **462**, 508 (2018).

⁴⁴ P.V. Yudin and A.K. Tagantsev. Fundamentals of flexoelectricity in solids. *Nanotechnology*, **24**, 432001 (2013).

⁴⁵ V.S. Mashkevich, and K.B. Tolpygo, *Zh.Eksp.Teor.Fiz.* **31**, 520 (1957). [*Sov.Phys. JETP*, **4**, 455 (1957)].

⁴⁶ Sh. M. Kogan, Piezoelectric effect under an inhomogeneous strain and an acoustic scattering of carriers of current in crystals *Solid State Physics* **5**, 2829 (1963).

⁴⁷ A. Kvasov, and A.K. Tagantsev, Dynamic flexoelectric effect in perovskites from first-principles calculations, *Phys. Rev.* **B 92**, 054104 (2015).

⁴⁸ M.D. Glinchuk, A.N. Morozovska, E.A. Eliseev. Ferroelectric thin films phase diagrams with self-polarized phase and electret state. *J. Appl. Phys.* **99**, 114102 (2006).

⁴⁹ M.D. Glinchuk, A.N. Morozovska. The internal electric field originating from the mismatch effect and its influence on ferroelectric thin film properties. *J. Phys.: Condens. Matter* **16**, 3517 (2004).

⁵⁰ Note that the surface coefficients e_{ijk}^s are usually renormalized by the δz lattice parameter that corresponds to the spacing between 2D layers, i.e., $e_{ijk}^s = \delta z e_{ijk}^b$, where e_{ijk}^b are in C/m².

⁵¹ A.N. Morozovska, E.A. Eliseev, A.K. Tagantsev, S.L. Bravina, L.-Q. Chen, and S.V. Kalinin. Thermodynamics of electromechanically coupled mixed ionic-electronic conductors: Deformation potential, Vegard strains, and flexoelectric effect. *Phys. Rev.* **B 83**, 195313 (2011).

-
- ⁵² See Supplementary Materials for calculation details, figures and STM results [URL will be provided by Publisher]
- ⁵³ N. Iguiñiz, R. Frisenda, R. Bratschitsch, and A. Castellanos-Gomez. Revisiting the buckling metrology method to determine the Young's modulus of 2D materials. *Advanced Materials* 31, 1807150 (2019). <https://doi.org/10.1002/adma.201807150>
- ⁵⁴ M. Ramos, J. Nogan, M. Ortíz-Díaz, J.L. Enriquez-Carrejo, C.A. Rodriguez-González, J. Mireles-Jr-Garcia, C. Ornelas, and A. Hurtado-Macias. Mechanical properties of RF-sputtering MoS₂ thin films. *Surf. Topogr.: Metrol. Prop.* 5, 025003 (2017).
- ⁵⁵ Y. Sun, J. Pan, Z. Zhang, K. Zhang, J. Liang, W. Wang, Z. Yuan, Y. Hao, B. Wang, J. Wang, and Y. Wu, Elastic properties and fracture behaviors of biaxially deformed, polymorphic MoTe₂. *Nano letters* 19, 761 (2019).
- ⁵⁶ L. Yu, Q. Yan, and A. Ruzsinszky. Negative Poisson's ratio in 1T-type crystalline two-dimensional transition metal dichalcogenides. *Nature communications* 8, article number: 15224 (2017).
- ⁵⁷ M. Yagmurcukardes, C. Sevik, and F.M. Peeters. Electronic, vibrational, elastic, and piezoelectric properties of monolayer Janus MoSTe phases: A first-principles study. *Phys. Rev. B* 100, 045415 (2019).
- ⁵⁸ K.-A.N. Duerloo, M.T. Ong, and E.J. Reed, Intrinsic piezoelectricity in two-dimensional materials, *J. Phys. Chem. Lett.* 3, 2871 (2012).
- ⁵⁹ Y. Jin, and J. Lee. First-principle Studies of Flexoelectric Effect in Corrugated Two-dimensional Materials. *Bulletin of the American Physical Society* 65, abstract: M65.00002 (2020).
- ⁶⁰ K.-A.N. Duerloo, Yao Li, and E.J. Reed. Structural phase transitions in two-dimensional Mo-and W-dichalcogenide monolayers. *Nat. Comm.* 5, article number 4214 (2014). DOI: 10.1038/ncomms5214
- ⁶¹ S. Song, D.H. Keum, S. Cho, D. Perello, Y. Kim, and Y. H. Lee. Room temperature semiconductor–metal transition of MoTe₂ thin films engineered by strain. *Nano letters* 16, 188 (2016). DOI: 10.1021/acs.nanolett.5b03481